



ELSEVIER

Ultramicroscopy 83 (2000) 193–216

---

---

ultramicroscopy

---

---

www.elsevier.nl/locate/ultramic

# The development of Fresnel contrast analysis, and the interpretation of mean inner potential profiles at interfaces

Rafal E. Dunin-Borkowski\*

*Center for Solid State Science, Arizona State University, Tempe, AZ 85287-1704, USA*

Received 8 January 1999; received in revised form 8 September 1999

---

## Abstract

This paper provides a summary of recent published and unpublished research on the development of Fresnel contrast analysis, a transmission electron microscopy technique for measuring the mean inner potential profile across an interface or a narrow layer. An algorithm for finding a best-fitting potential profile is described, energy-filtered experimental data are analyzed and contributions to Fresnel contrast from surface grooves and space charge are assessed. Many of the conclusions drawn are equally relevant for the interpretation of phases measured using off-axis electron holography. © 2000 Elsevier Science B.V. All rights reserved.

**Keywords:** Fresnel contrast; Mean inner potential; Interfaces

---

## 1. Introduction

The mean inner potential profile across a grain boundary, a flat precipitate or a semiconductor quantum well can provide highly useful information about variations in composition, density and ionicity across the layer, as well as about built-in potentials associated with depletion layers or space charge. Transmission electron microscopy (TEM) techniques for measuring local variations in potential are based on the formation of phase contrast, and as such can all be classified as branches of holography. This paper provides a review of some recent developments in Fresnel contrast analysis,

a technique that involves the acquisition of a through-focal series of images of a narrow layer using coherent illumination and an objective aperture that typically encloses no diffracted beams [1]. Each image in a Fresnel defocus series is strictly an in-line electron hologram [2,3], in which an interference pattern is formed at the position of the layer. The way in which this interference pattern changes with objective lens defocus is compared with computer simulations to determine the mean inner potential profile of interest. In contrast to off-axis electron holography [4,5], Fresnel contrast can only provide the local *variation* in potential at an interface (and not its magnitude) because the interference pattern is formed from waves that have all passed through the sample, rather than from interference between a vacuum wave and a sample wave. However, the technique has the advantage that it can be applied in a TEM that has neither a biprism nor a field emission gun, and the defocus

---

\* Correspondence address: Department of Materials, Parks Road, Oxford OX1 3PH, UK.

E-mail address: rafal.db@materials.ox.ac.uk (R.E. Dunin-Borkowski)

and aberrations of the electron microscope are also automatically removed from the fitted potential profile. (They would still be present in the phase of a single off-axis electron hologram.)

The recent developments in Fresnel contrast analysis that are described here center on the use of an automated minimization algorithm to improve the accuracy to which potential profiles can be determined from experimental Fresnel defocus series. Such a fitting routine is much more straightforward to apply to Fresnel fringes than to high-resolution electron microscope (HREM) images because the contrast changes more slowly with both specimen thickness and defocus. For example, there are no periodic contrast reversals with either specimen thickness or defocus. The width and the shape of a potential profile are also related to specific features of the contrast such as the spacing and the contrast of the Fresnel fringes. The analysis of energy-filtered images provides the further benefit of allowing data to be compared quantitatively with simulations without the need to model inelastic scattering. In this context, both the spatial resolution of Fresnel contrast analysis and the uniqueness of the fitted potential are discussed. An approach that allows the effects of surface grooves to be identified and removed from a measured potential profile is also presented, and the magnitude of the fringing field surrounding a thin foil that contains a space charge layer is assessed. Both of these effects are potentially important because they can alter a measured potential from the form that it would have in the bulk material.

## 2. Experimental details and background to Fresnel contrast analysis

### 2.1. Experimental details

Energy-filtered images were obtained using a JEOL 4000FX microscope ( $C_s = 2.0$  mm), equipped with a post-column Gatan imaging filter (GIF) and operated at 400 keV. A 10 eV energy window, centered on the zero-loss peak, was used for filtered imaging. Unfiltered data were also obtained at 200 keV using a JEOL 2000FX ( $C_s = 2.3$  mm) and at 300 keV using a Philips CM30 ( $C_s = 2.0$  mm)

microscope. In common with most TEM techniques that involve matching experimental contrast with simulations, imaging parameters such as objective aperture size, beam convergence, defocus step size and magnification were calibrated accurately. The specimen thickness of each area of interest was also measured, either using weak-beam dark field thickness fringes or from a ratio of energy-filtered to unfiltered intensity (see below). Images captured on film were digitized using a Scandig-Joyce LoebI rotating drum densitometer at a resolution of 25  $\mu\text{m}$ / pixel and scaled to linearity in electron dose using a measured emulsion response curve. Images acquired digitally using a charge-coupled device camera were always processed to remove the point-spread function of the detector. Image processing, simulation and the determination of best-fitting potential profiles were all carried out using Semper [6] software on a Silicon Graphics workstation.

### 2.2. Background to the technique

Ever since the first detailed studies of Fresnel contrast at interfaces by Bursill et al. [7] and Ruhle and Sass [8], the analysis of experimental data has involved plotting graphs of fringe contrast and spacing as a function of defocus to obtain matches with simulations e.g. Refs. [9–13]. The basic approach involves acquiring a defocus series of the layer of interest, such as that shown for two grain boundaries in mullite in Fig. 1a [14], using an objective aperture that encloses only the zero beam and part of the diffuse streak formed by scattering from the interface. Qualitatively, if the central Fresnel fringe is bright underfocus then the mean inner potential of the layer is lower than that of the surrounding material, while if it is dark underfocus then the potential is higher. One-dimensional fringe profiles are obtained by projecting the intensities of small regions of known thickness parallel to the direction of the layer and dividing each of these by a constant background [1]. The spacing and contrast of the resulting fringes, which are defined using the symbols shown in Fig. 1b, are then compared with simulations using graphs plotted as a function of defocus (Figs. 1c and d). (*Absolute intensities* are still very rarely compared with simulations.)

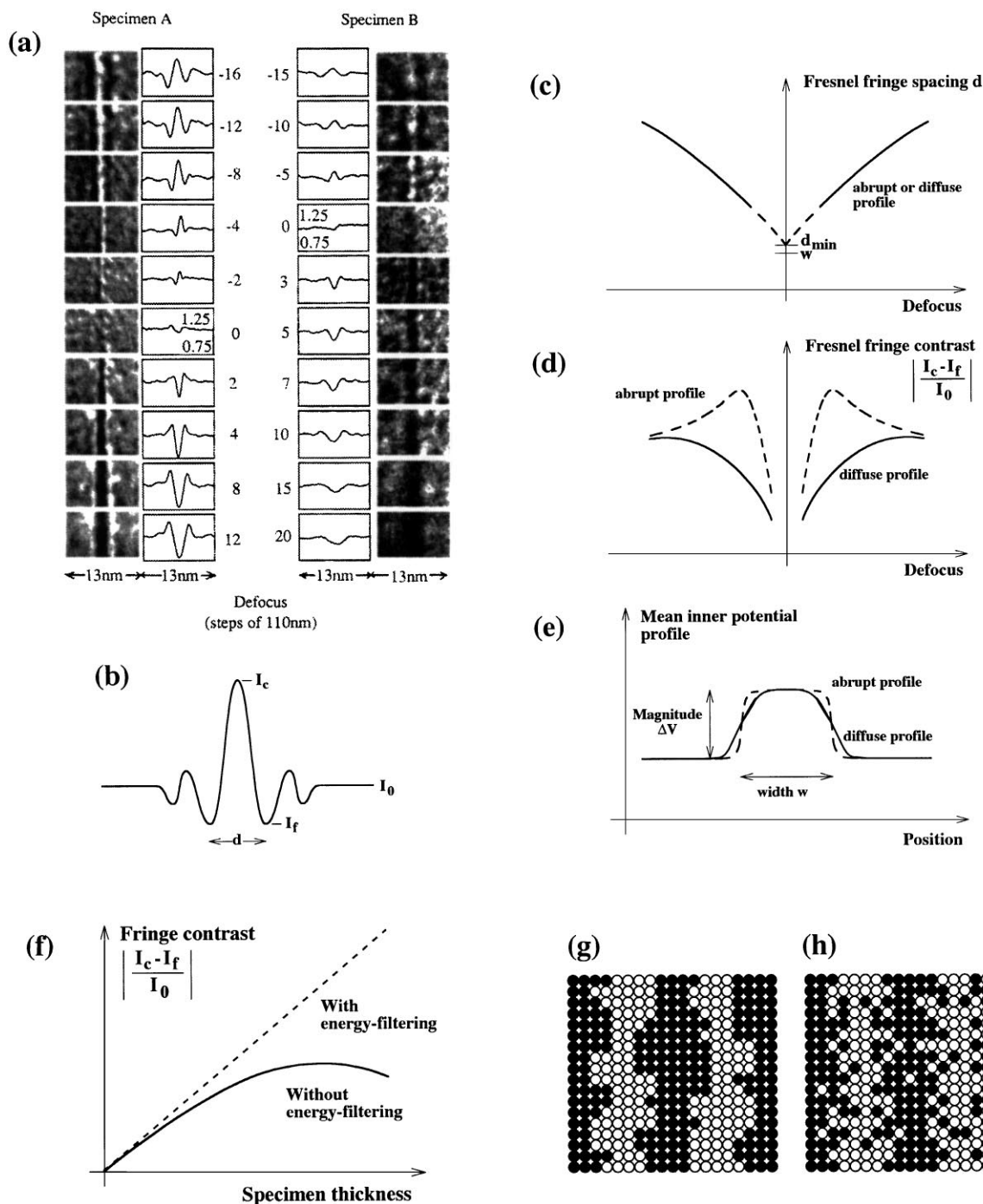


Fig. 1. (a) Fresnel defocus series of two mullite grain boundaries for identical specimen thicknesses, alongside corresponding line profiles averaged along layer directions. (See Ref. [14] for details); (b) symbols used to define Fresnel fringe contrast and spacing; Schematic graphs of (c) fringe spacing and (d) fringe contrast as function of defocus for abrupt and diffuse interfaces; (e) schematic mean inner potential profiles corresponding to graphs in c and d; (f) schematic diagram of fringe contrast at a given defocus as function of specimen thickness with and without energy-filtering; Schematic diagrams of (g) rough and (h) diffuse interfaces.

The fringe spacing extrapolates to a minimum value slightly larger than the true width of the potential profile (Fig. 1e), while the variation in contrast with defocus is used to determine its magnitude and shape. The simulations usually incorporate one-dimensional multislice calculations that include only the background potential underlying that of the atoms (Fig. 1e). The best-fitting potential profile is interpreted using the expression [1]

$$V_0 = \left( \frac{h^2}{2\pi m e \Omega} \right) \sum_{\text{unit cell}} f_{\text{el}}(0), \quad (1)$$

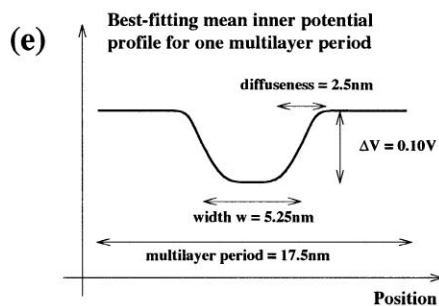
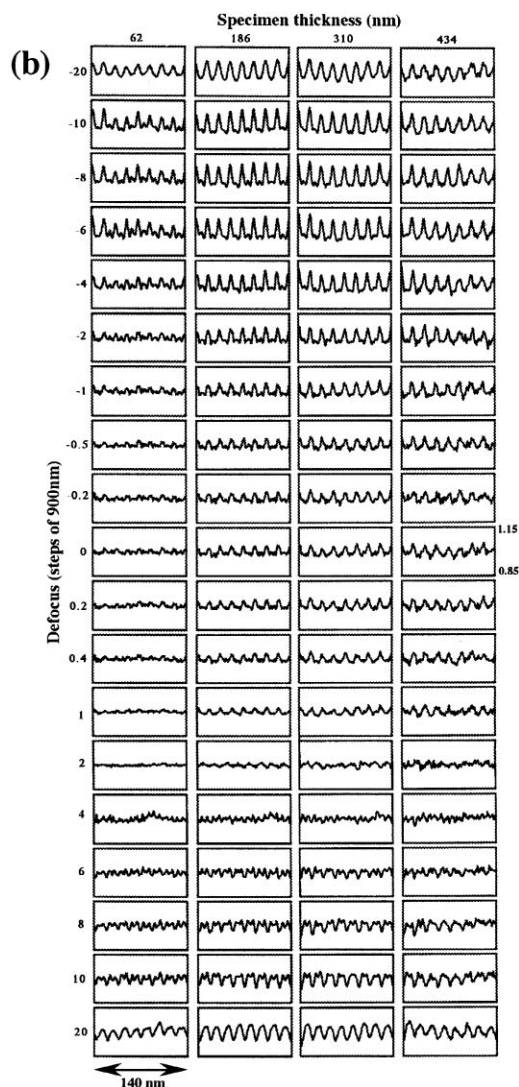
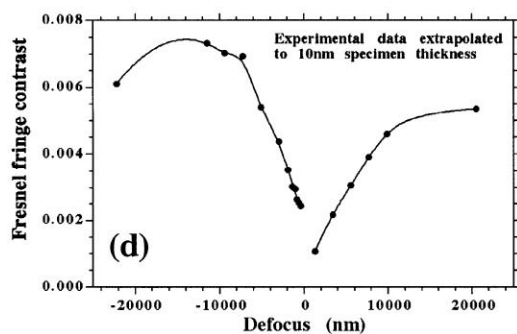
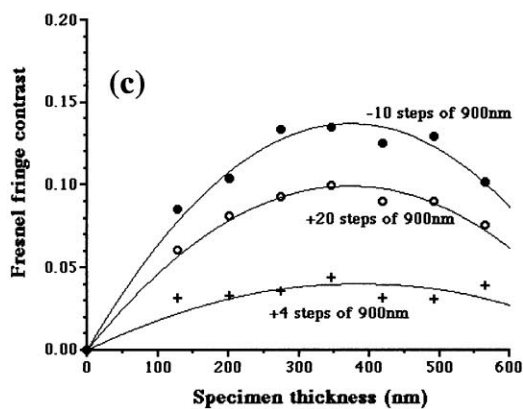
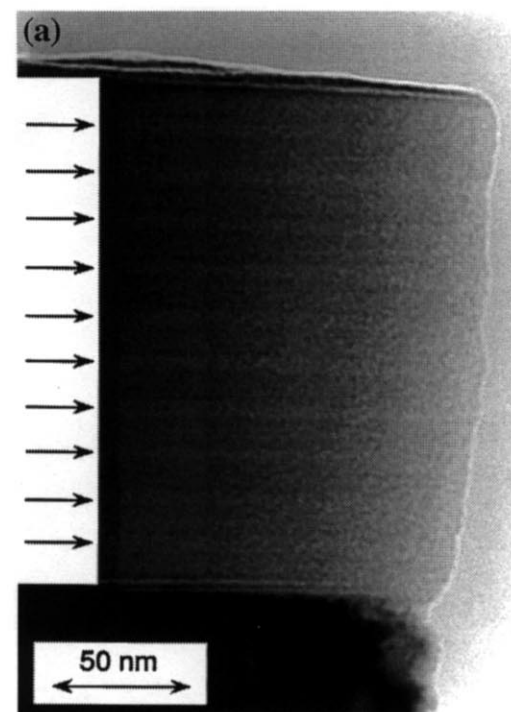
which relates the mean inner potential  $V_0$  to changes in density and composition through the parameters  $\Omega$  (the unit cell volume) and  $f_{\text{el}}(0)$  (the electron scattering factor of an atom or ion at zero scattering angle) [15,16], respectively. If unfiltered images are analyzed, then the measured contrast falls below that predicted theoretically as a result of inelastic scattering into the objective aperture used (Fig. 1f). The detailed form of this scattering is difficult to calculate with confidence [1,17–19], and the only reliable procedure is to remove the inelastically scattered electrons by energy-filtering. Commercial imaging spectrometers are now available, and their application to Fresnel contrast will be described below. A fitted potential profile cannot be used to distinguish between roughness (Fig. 1g) and true chemical interdiffusion (Fig. 1h) at an interface. However, an analysis of the apparent waviness of the contrast along the interface can be used to provide this information if the specimen thickness is known [20]. It should also be emphasized that a single defocused image cannot be matched uniquely [21], while greater confidence in the fitted potential is provided by acquiring a larger number of images in the defocus series.

### 2.3. Quantitative Fresnel contrast analysis in the absence of energy-filtering

Before applying a fitting algorithm to analyze energy-filtered data, a possible approach for removing the effects of inelastic scattering in the absence of an energy-filtering microscope will be outlined. This approach can be applied to samples that have a monotonic and well-characterized

variation in specimen thickness, and involves extrapolating the fringe contrast at each defocus to a thickness at which inelastic scattering is negligible, but at which the contrast would be too small to measure. Fig. 2a shows one member of an unfiltered Fresnel defocus series of a superlattice that contains alternating layers of high-density amorphous hydrogenated carbon with similar compositions and densities but different band gaps (the narrower, lower band-gap layers are marked). The image shown is 5400 nm underfocus and was obtained at 300 keV using an objective aperture of semi-angle 3 mrad, with a measured beam convergence semi-angle of 0.12 mrad. The layers were grown directly onto {0 0 1} Si and the sample was prepared by cleaving the Si at a 90° wedge angle. The thickness profile of the amorphous layers has followed the cleave, allowing Fresnel fringe profiles to be obtained at several known specimen thicknesses (Fig. 2b). The contrast at each defocus can be extrapolated as a function of specimen thickness (Fig. 2c), in this case to a thickness of 10 nm, and plotted for quantitative comparison with simulations without the need to include the effects of inelastic scattering (Fig. 2d). The best-fitting potential profile to the contrast in Fig. 2d is shown in Fig. 2e. A detailed examination of this profile, in combination with electron energy loss data, confirmed the presence of different proportions of  $\pi$  bonding in adjacent layers, which are in turn associated with differences in local ordering. This interpretation, which provides an understanding of the origin of the different bandgaps in the layers and is explained in detail elsewhere [22], highlights the fact that  $V_0$  is the most sensitive parameter to the redistribution of electrons due to bonding [23,24].

Fig. 2. (a) One member of Fresnel defocus series of multilayer of alternating layers of amorphous hydrogenated carbon, taken 5400 nm underfocus, with Si substrate at bottom and vacuum at top. Specimen thickness increases from right to left. Lower band-gap layers are arrowed; (b) line profiles of Fresnel contrast as function of defocus for several specimen thicknesses; (c) extrapolation of fringe contrast to zero specimen thickness for three defoci; (d) fringe contrast extrapolated to 10 nm specimen thickness for each defocus; (e) best-fitting potential profile to extrapolated Fresnel fringe contrast with narrower, lower band-gap layer at center.



### 3. Application of a fitting algorithm to Fresnel contrast

#### 3.1. An automated fitting routine

The disadvantage of an analysis of the type shown in Figs. 1 and 2 is that only three data points from each image are compared with simulations. This section demonstrates the use of a multi-parameter minimization algorithm to obtain a best fit to every pixel in an experimental defocus series. The sequence of input parameters required for the fitting routine used here, which incorporates a standard Simplex algorithm [25], is listed in the appendix. Some of these parameters (e.g., specimen thickness, defocus step size and objective aperture size) are experimentally measured values that are assumed to be accurate. Others (e.g., the dimensions of the potential well or barrier) are initial guesses, whose values are fitted by the algorithm by matching the experimental and simulated defocus series iteratively while varying each such parameter in turn. Each iteration involves the creation of a new potential profile whose shape is specified using three parameters that describe its width, depth and shape (see below) and the evaluation of a (typically  $256 \times 1$  pixel) multislice calculation. (Although only Gaussian-shaped profiles are included in the simulations, in principle these could be distinguished experimentally from the linearly -graded profiles used in previous work, e.g., Ref. [1]). A goodness-of-fit criterion (here, the mean-squared difference between the experimental and simulated defocus series) is then used to compare the experimental and simulated defocus series. Beam convergence, absorption and the starting defocus value for the series are also fitted by the algorithm, as errors in these parameters affect the fitted potential. For example, an incorrect value of beam convergence can affect both the depth and the shape of the fitted potential. Similarly, an incorrect value of starting defocus can affect the fitted absorption, which is modeled by including an imaginary part (*directly* proportional to the real part) of the scattering potential [26]. Absorption describes the variation in intensity scattered outside the objective aperture, a higher value indicating greater scattering to large angles. The specimen thickness, objective aperture

size, accelerating voltage, defocus step size, spherical aberration coefficient and focal spread are all assumed to be known exactly, and physical constraints are included to ensure that parameters such as beam convergence cannot go below zero. Several starting configurations of well width, shape and depth can be used to confirm that a global minimum has been found; a poor fit is usually obvious visually if the algorithm converges to a local minimum, and the program can then be restarted from different parameters. (The use of more than three parameters to specify the shape of a potential profile in a fitting algorithm would increase the difficulty of finding a global minimum.) The accuracy of the fit is, in practice, limited primarily by the accuracy to which the specimen thickness of the area of interest can be measured.

#### 3.2. Application to simulated Fresnel defocus series

Figs. 3a and b illustrate the application of the fitting algorithm to two simulated Fresnel defocus series, starting from estimates of the beam convergence and defocus that differ from the true values by amounts that are representative of errors in measurements of these parameters. The calculations are performed for an accelerating voltage of 200 keV, a spherical aberration coefficient of 2 mm, an objective aperture semi-angle of 4.2 mrad, a focal spread of 15 nm and a defocus step size of 200 nm. The left side of each figure contains the simulated Fresnel defocus series displayed both as individual line profiles and as a montage with defocus along the  $y$ -axis. (Other authors [27] have displayed such profiles side-by-side.) The real and imaginary parts of the potentials that were used to generate the profiles are also shown. The right side of each figure contains the initial and final stages of the fitting algorithm, in the form of the current best guess for the potential profile and the corresponding defocus series (again, displayed as a montage). The match between the input to the calculation and the best-fitting potential profile is near-perfect in both Fig. 3a, which contains a potential well that is more diffuse in shape, and Fig. 3b, in which the potential barrier has steeper sides. In Fig. 3b, a barrier with walls that are abrupt to within 0.2 nm was fitted perfectly even though the objective aperture

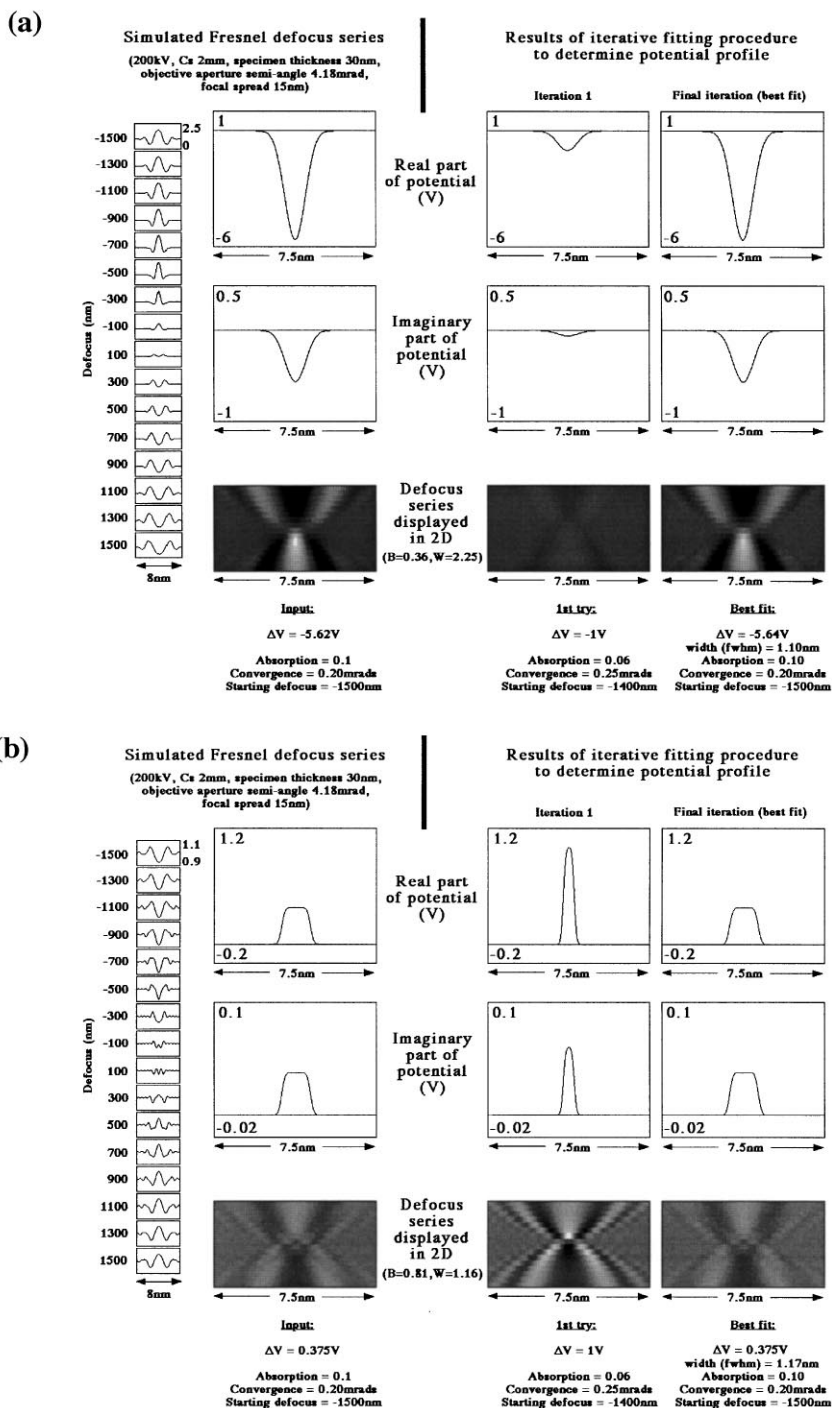


Fig. 3. Application of fitting algorithm to simulated Fresnel defocus series for (a) diffuse potential well and (b) abrupt potential barrier. Both real and imaginary part of potential, and Fresnel fringe contrast (in a single picture with defocus as y-axis) are plotted for simulated series and for first and last iteration of fitting algorithm. Imaging and fitting parameters are given below figures.

had an Airy disc diameter of 0.73 nm. However, it should be noted that the simulated and fitted potentials were generated from functions that have the same form (top hats smoothed using Gaussian functions); information excluded by the small objective aperture may thus be specified uniquely once the spatial frequencies admitted by the aperture are determined from the Fresnel data. For a potential profile of unknown shape, the concept of the “resolution” of the potential recovered using Fresnel contrast may require an analysis using the theory of analytic continuation [28], particularly in the presence of dynamical scattering back into a small aperture. In this situation, a fitting routine may simply return a best-fitting function to the true potential profile. The resolution of a potential profile provided by analyzing the Fresnel fringes in an HREM image obtained with an aperture large enough to enclose diffracted beams [29] would be conceptually easier to understand.

### 3.3. Application to energy-filtered experimental data, and the measurement of sample thickness

Fig. 4 contains an example of the application of the fitting algorithm to energy-filtered data obtained at 400 keV from three single crystalline Fe/Cu multilayers grown on [001] Cu, in which the Fe is sufficiently thin to have a face-centered tetragonal rather than the usual body-centered structure. Such multilayers exhibit anomalous elastic and magnetic properties, and a knowledge of their atomic and electron structures is important for understanding effects such as giant magnetoresistance. Each multilayer has a periodicity of  $\sim 3$  nm and contains 100 repeat units (Fig. 4a). The nominal structures are  $\text{Fe}_2/\text{Cu}_{15}$ ,  $\text{Fe}_4/\text{Cu}_{13}$  and  $\text{Fe}_6/\text{Cu}_9$  in units of atomic layers (AL). Examples of images taken from Fresnel defocus series of the  $\text{Fe}_2/\text{Cu}_{15}$  sample (in which the thinner Fe layers show contrast characteristic of a potential barrier) are shown in Figs. 4b and c for defocus values of 240 and  $-240$  nm, respectively. Such layers could not be characterized using HREM as a result of the similar atomic numbers of the elements present (Fig. 4d). Figs. 4e, f, g show experimental Fresnel fringe profiles from three multilayer periods of the  $\text{Fe}_2/\text{Cu}_{15}$ ,  $\text{Fe}_4/\text{Cu}_{13}$  and  $\text{Fe}_6/\text{Cu}_9$

samples for measured specimen thicknesses of 59, 32 and 43 nm, respectively. The Fresnel line profiles are visibly different in both magnitude and detail between the three sets of data. Alongside each column of experimental data are the best-fitting simulated profiles generated by the fitting algorithm. The real parts of the fitted potential profiles are shown in Figs. 4h–j. Potential profiles measured from several different specimen thicknesses are shown for each sample; the slightly different results obtained for different specimen thicknesses from the same sample reflect in part the degree to which the specimen thickness can be measured accurately. Small tilts of the layers from the vertical also contribute to the slightly different projected widths for the profiles obtained from different sample thicknesses (see below). Confidence in the fitted profiles in Figs. 4h–j is provided by their monotonic change with increasing Fe layer thickness. A similar gradual change is observed on annealing the 6 Fe AL sample sequentially at 720 K for 10 min (h1), 720 K for 80 min (h2) and 800 K for 30 min (h3) (Fig. 4k). A detailed examination of the potential profiles in Figs. 4h–k was used to show that the Fe exhibits a layer thickness dependent tetragonal distortion, which is inconsistent with the predictions of continuum elasticity theory if the bulk elastic properties of Fe are assumed. This study is presented in full elsewhere [30,31].


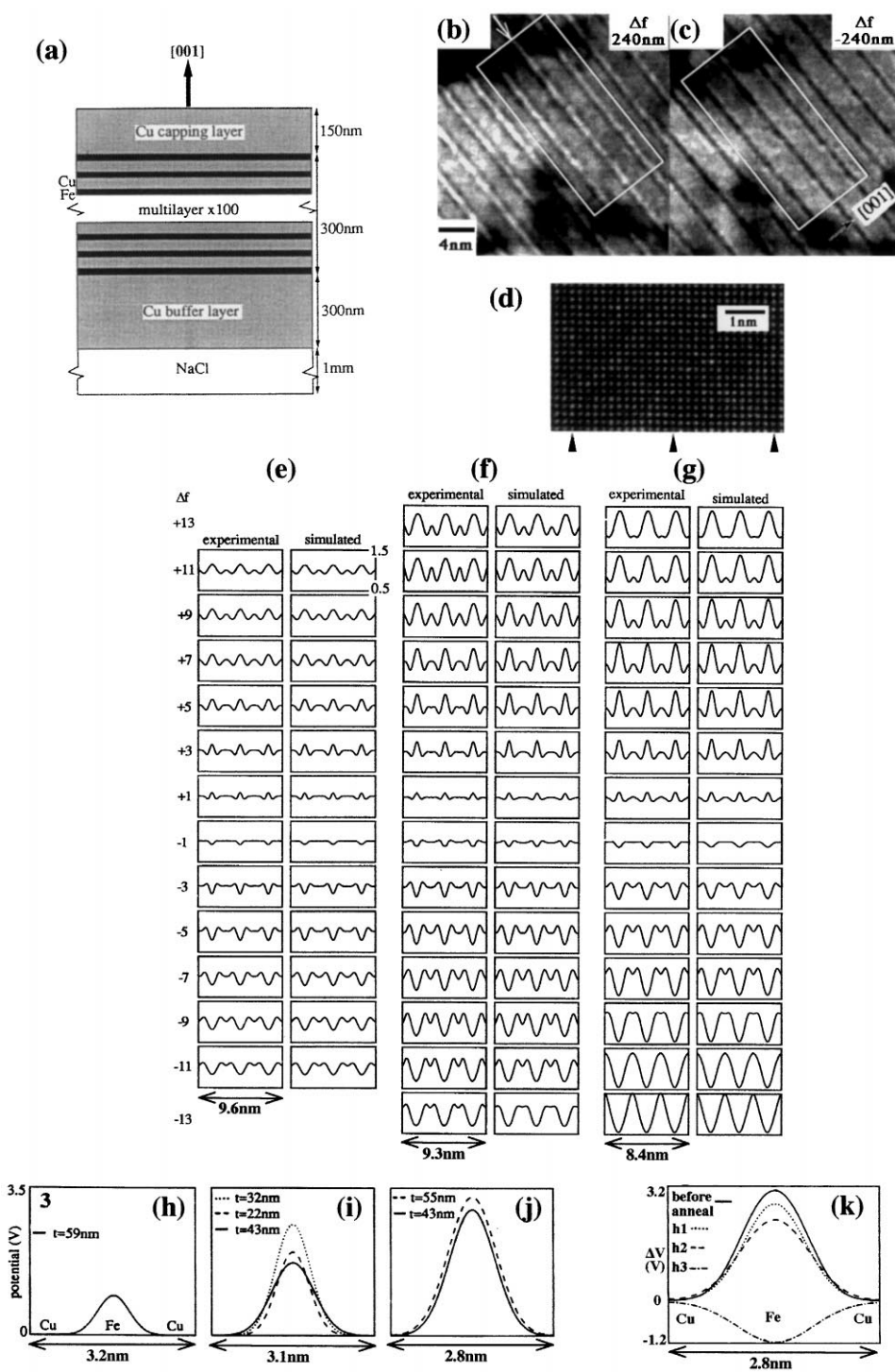


Fig. 4. Application of fitting algorithm to experimental Fresnel contrast from three single-crystal Fe/Cu multilayers on [001] Cu. (a) Schematic diagram of layer structures; (b) and (c) two members of Fresnel defocus series of  $\text{Fe}_2/\text{Cu}_{15}$  multilayer at defocus values indicated. Line profiles were obtained by projecting contrast in boxed regions in direction of white arrow; (d) non-axial HREM image from Fe/Cu multilayer structure. Positions of centers of Fe layers (each of which is several atomic layers in thickness) are marked; (e), (f) and (g) experimental Fresnel defocus series from three different multilayers whose layer structures are  $\text{Fe}_2/\text{Cu}_{15}$ ,  $\text{Fe}_4/\text{Cu}_{13}$  and  $\text{Fe}_6/\text{Cu}_9$  for specimen thicknesses of 59, 32 and 43 nm, respectively, alongside best-fitting simulated defocus series from fitting algorithm; (h), (i) and (j) best-fitting potential profiles to experimental data for  $\text{Fe}_2/\text{Cu}_{15}$ ,  $\text{Fe}_4/\text{Cu}_{13}$  and  $\text{Fe}_6/\text{Cu}_9$  multilayer structures, respectively. Data from several specimen thicknesses are shown for each multilayer; (k) Best-fitting potential profiles for  $\text{Fe}_6/\text{Cu}_9$  multilayer as function of annealing temperature. h1, h2 and h3 correspond to annealing thin foil at 720 K for 10 min, 720 K for 80 min and 800 K for 30 min, in sequence.





Weak-beam dark-field imaging could not be applied to the Fe/Cu samples, and so the sample thickness was measured from intensities in unfiltered and energy-filtered images ( $I_{\text{tot}}$  and  $I_{\text{el}}$ ) using

$$\left(\frac{t}{\lambda_{\text{in}}}\right) = \ln\left(\frac{I_{\text{tot}}}{I_{\text{el}}}\right), \quad (2)$$

where  $\lambda_{\text{in}}$  is the total inelastic mean-free path [32]. This approach requires great care both in the choice of  $\lambda_{\text{in}}$  and if amorphous surface layers are present. The latter point is explained in Fig. 5 in the form of line profiles obtained at 400 keV from a similar Fe/Cu sample to that analyzed in Fig. 4. Data are presented for a single defocus value, both with and without energy-filtering, and with and without the use of an objective aperture of semi-angle 4.5 mrad. The application of Eq. (2) to the line profiles in Fig. 5a would result in the apparent specimen thickness profile shown as a dotted line in Fig. 5b. However, simple algebra shows that in the presence of an amorphous surface layer of total thickness  $t_{\text{am}}$  and inelastic mean free path  $\lambda_{\text{in(am)}}$  Eq. (2) in fact provides a measured thickness closer to

$$\left(\frac{t}{\lambda}\right)_{\text{effective}} = \left(\frac{t}{\lambda_{\text{in}}}\right) + \left(\frac{t_{\text{am}}}{\lambda_{\text{in(am)}}}\right)$$

than to the desired parameter  $\left(\frac{t}{\lambda_{\text{in}}}\right)$ . (3)

A better approximation to the true crystal thickness can be obtained by scaling each of the line profiles in Fig. 5a to unity at the interface between the crystal and the amorphous surface layer before applying Eq. (2). The resulting thickness profile is shown as a continuous line in Fig. 5b and, as expected from Eq. (3), the solid and dotted lines differ by a constant value within the crystal. The thickness of the crystal that contributes to the measured Fresnel contrast would thus be overestimated dramatically if Eq. (2) were applied without taking account of the presence of the surface layer. Profiles such as those shown in Fig. 5a are also useful for determining the ratio of elastic to inelastic mean free path within the material (Figs. 5c and d).

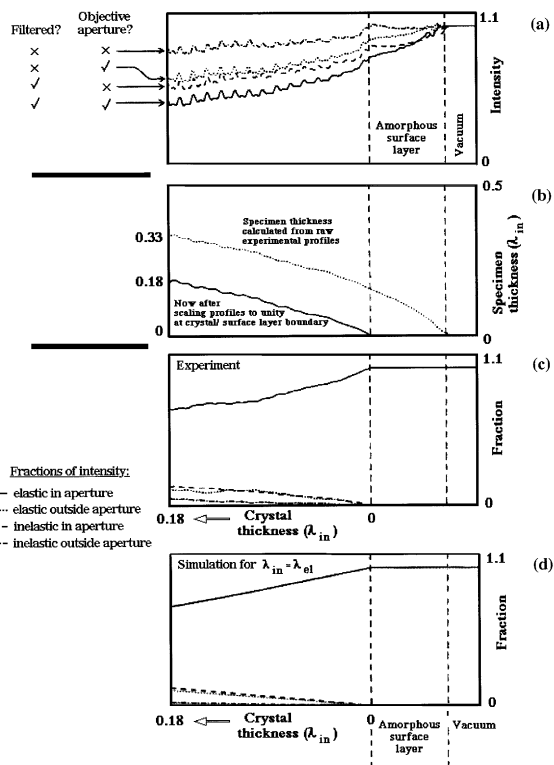


Fig. 5. (a) Line profiles as function of distance into sample for Fe/Cu multilayer, both with and without energy-filtering and with and without objective aperture of semi-angle 4.5 mrad; (b) specimen thickness in units of total inelastic mean-free path calculated from ratio of filtered to unfiltered intensity, before and after scaling intensities at boundary of crystal and surface layer to unity. (similar results are obtained using profiles with and without objective aperture); (c) fractions of elastic and inelastic intensity inside and outside objective aperture calculated from smoothed versions of profiles in (a); (d) corresponding simulation for equal elastic and inelastic total mean free paths.

### 3.4. Future applications

Two examples of problems that would benefit from a fitting algorithm that includes a fully atomistic calculation at each iteration, rather than the continuum approach outlined above, are now briefly described. Fig. 6 shows the application of Fresnel contrast analysis to a layer of InAsP formed by interrupting the growth of [0 0 1] InP and subjecting the surface to an As flux for 32 s (Fig. 6a) [33]. Two images of a 90° cleaved wedge sample

containing the layer are shown in Figs. 6b and c for defocus values of 7800 and  $-8200$  nm, respectively. No orientation could be found at which the layer was vertical and the sample weakly diffracting as a result of the large 200 structure factor of InP. As a result, atomistic models had to be used to match the experimental contrast with simulations. Experimental fringe profiles (Figs. 6d and e) were compared with simulations (Figs. 6f and g) both as absolute intensities relative to a vacuum level of unity and after dividing each profile by a constant background, with each supercell describing the variation in As concentration generated by hand. (This is the only example in this paper in which the absolute intensities as well as the contrast of experimental data are compared with simulations). Both the As concentration at the center of the layer and absorption parameters were determined by matching intensity profiles plotted as a function of specimen thickness (Figs. 6h and i) to simulations. The width and the shape of the compositional profile were then determined from the Fresnel fringe profiles (Figs. 6d and e). The best-fitting compositional profile (Fig. 6j) corresponds to a maximum As concentration of 60 at%, a mean layer width of 1.8 nm and diffuse interfaces. Such a comparison of an entire thickness–defocus series with simulations results in great sensitivity when determining the compositional profile. However, discrepancies are still present and an iterative modification of the atomistic potential profiles would be much more efficient using an automated fitting procedure.

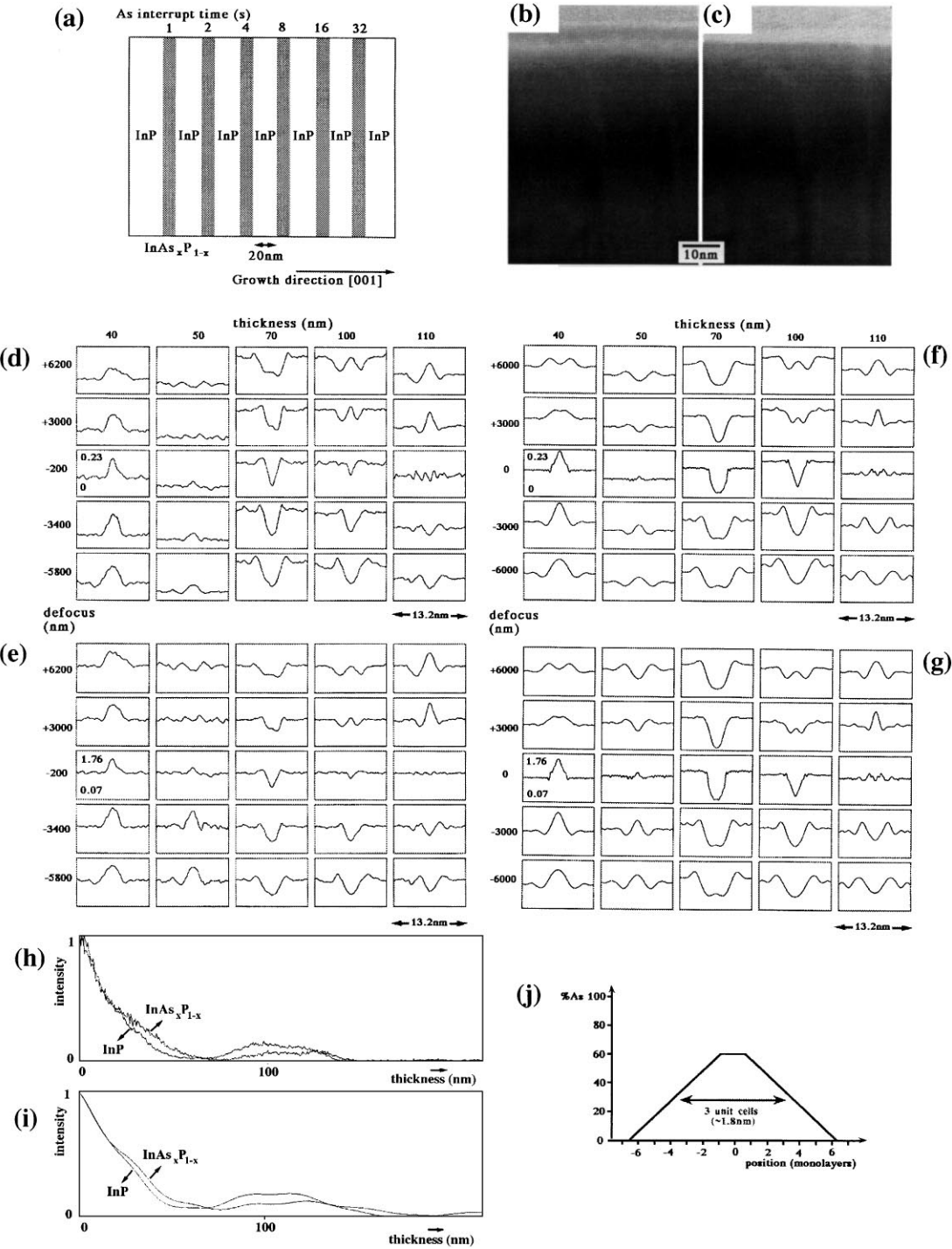
Fig. 7a shows a bright field image of a sample that contains nominally a full monolayer and a full bilayer of Si, grown 50 nm apart on  $[001]$  GaAs. The image was obtained 600 nm underfocus at 200 keV, at a systematic row orientation approximately  $7^\circ$  from  $[100]$ . The beam convergence and objective aperture semi-angles are 0.4 and 3.5 mrad, respectively. The potential profiles of the layers can be generated from bright-field Fresnel contrast in a standard way (each layer has in fact spread over two GaAs unit cells), however additional information can be obtained through the examination of dark-field Fresnel contrast. (An entire defocus series rather than a single image [34] must again be analyzed.) One member of such a series, obtained 600 nm underfocus at a  $g = 002$

diffracting condition with a positive deviation parameter, again using a 3.5 mrad aperture, is shown in Fig. 7b. The dark-field contrast is particularly sensitive to the site occupancy of the Si atoms on the GaAs lattice. Figs. 7c and d show experimental dark-field Fresnel contrast profiles for a specimen thickness of 40 nm, which exhibit clear dark contrast overfocus for both layers. The atomistic computer simulations shown in Figs. 7e–h were performed for one full monolayer (1 ML) or four full monolayers (4 ML) of Si located on Ga or both Ga and As sites. The data provide a much closer match to the simulations for Si located on both Ga and As sites [35], independent of the amount of strain included in the simulations. However, discrepancies (e.g., the reversal in contrast of the experimental profiles with defocus, which is not reproduced in the simulations) are again evident, and a more efficient method of matching such data is required.

#### 4. Surface grooves, space charge, and the presence of free surfaces

##### 4.1. Surface grooves and interface tilt

Surface grooves may form at certain types of boundary as a result of differential thinning during specimen preparation [36,37]. Any boundary may also be wavy or tilted within the foil thickness [38]. An approach for detecting the effects of surface grooving or interface tilt is illustrated in Fig. 8. This approach is based on the assumption that TEM techniques measure a volume-averaged potential projected in the incident beam direction and relies on the measurement of potential profiles at several specimen thicknesses. The true potential profile has a width  $w$  and a depth  $(V_1 - V_2)$ , where  $V_1$  and  $V_2$  are the mean inner potentials of the matrix and layer, respectively, whereas the measured profile has a thickness-dependent width  $d$  and depth  $\Delta V$ . The schematic diagrams in the second and third rows of Fig. 8 show two extreme limits for the forms of surface grooves alongside a diagram of a layer that is tilted from the vertical by a small angle  $\alpha$ . The thicknesses of the samples measured using a technique such as weak-beam dark-field imaging



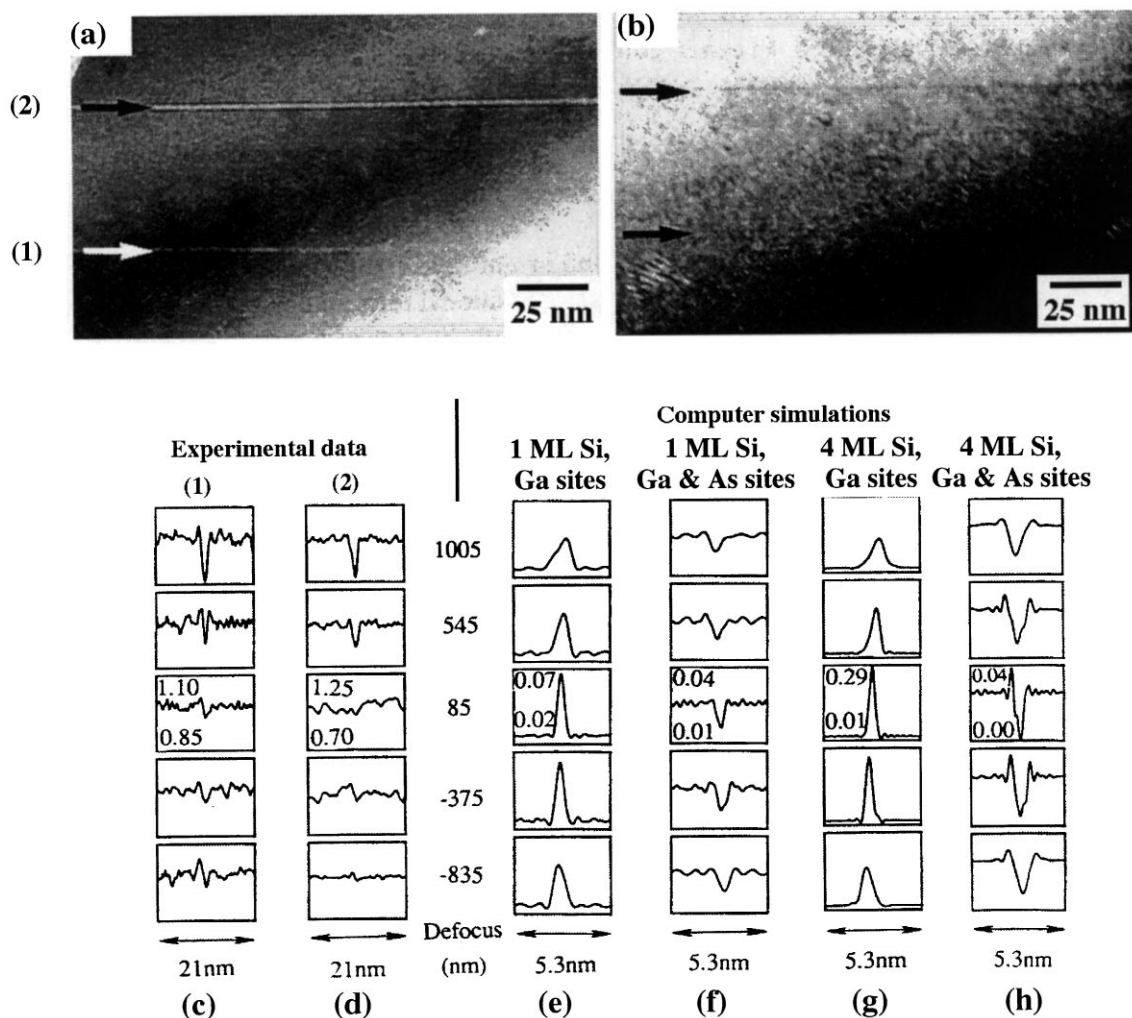


Fig. 7. (a) Bright field image of (1) Si monolayer and (2) Si bilayer, grown 50 nm apart on  $[0\ 0\ 1]$  GaAs, taken 600 nm underfocus; (b) dark-field image in  $g = 002$  diffracting condition with positive deviation parameter, also 600 nm underfocus; (c) and (d) experimental dark-field Fresnel contrast profiles from Si monolayer and bilayer, respectively. (e)–(h) atomistic simulations of dark-field Fresnel contrast for one full monolayer (1 ML) or four full monolayers (4 ML) of Si spread over 2 unit cells on either Ga sites or both Ga and As sites.

Fig. 6. (a) Schematic diagram of InP structure containing InAsP layers formed by interrupting growth under As flux for times indicated; (b) and (c) energy-filtered images of As layer for 32s interrupt time for defocus values of +7800 and -8200 nm, respectively; Experimental Fresnel defocus series as function of specimen thickness and defocus displayed (d) as raw data with vacuum intensity of unity and (e) after dividing each profile by a uniform background; (f) and (g) best-fitting simulated profiles to experimental series (d) and (e), respectively; (h) intensity as function of specimen thickness for bulk InP and for center of InAsP layer; (i) Best-fitting simulated profiles to experimental data in h; (j) Best-fitting compositional profile to experimental data in d–i.

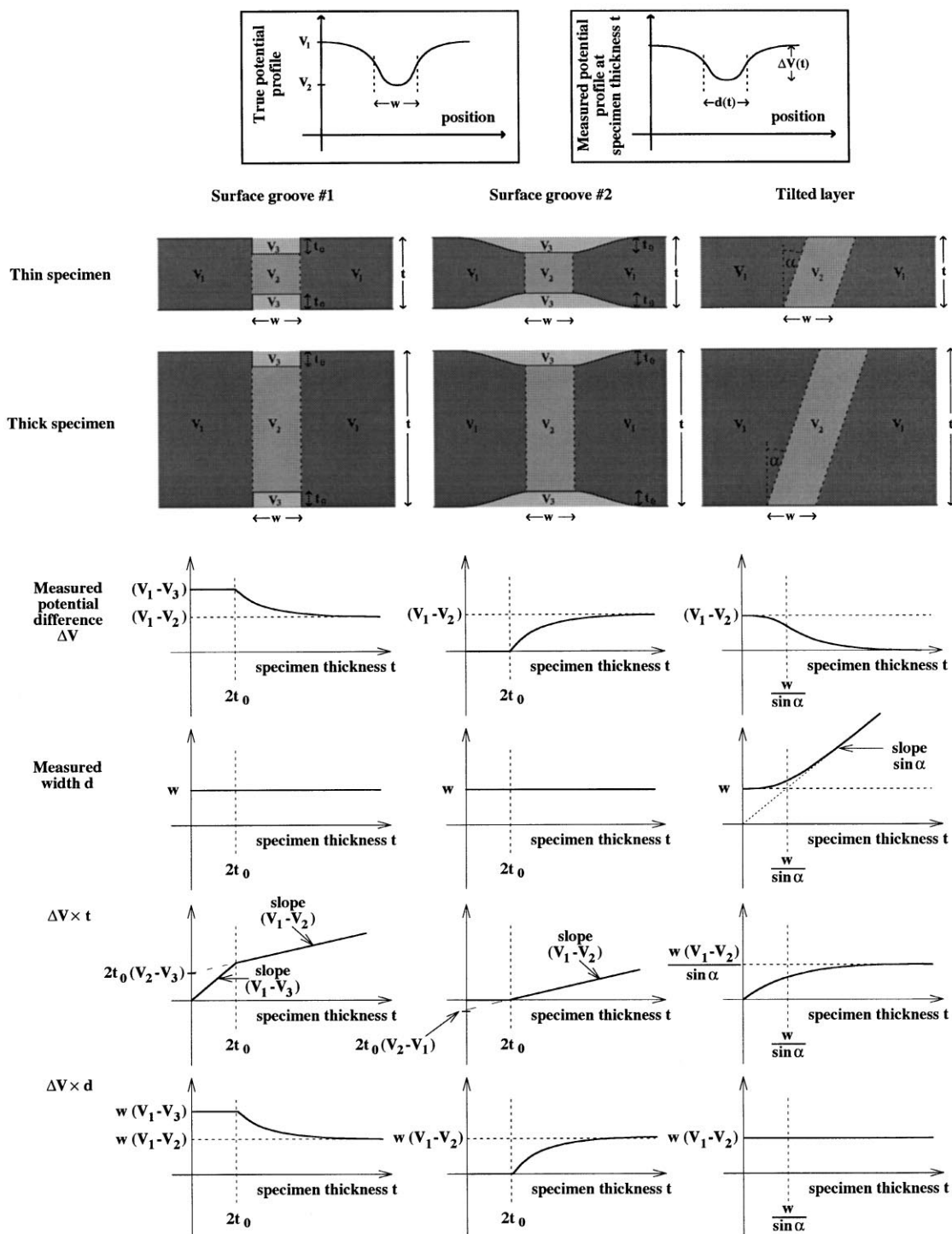


Fig. 8. Schematic diagrams showing effect of two different forms of surface groove and a tilted layer on width and depth of measured potential profile, as function of specimen thickness. (See text for details). Graphs are drawn for mean inner potentials  $V_1 > V_2 > V_3$ .  $V_3$  would be zero for groove that is not filled in.

would be  $t$ . Each surface groove has a depth  $t_0$  and contains an unknown material of inner potential  $V_3$ . For the groove of width  $w$ , below a thickness of  $2t_0$  only the material with potential  $V_3$  is present in the boundary and  $\Delta V$  is equal to  $(V_1 - V_3)$ . For higher specimen thicknesses,

$$\begin{aligned}\Delta V &= \left(\frac{2t_0}{t}\right)(V_1 - V_3) + \left(\frac{t - 2t_0}{t}\right)(V_1 - V_2) \\ &\equiv (V_1 - V_2) + \left(\frac{2t_0}{t}\right)(V_2 - V_3),\end{aligned}\quad (3a)$$

which tends towards  $(V_1 - V_2)$  for  $t \gg 2t_0$ . In contrast, if an interlayer with a wide groove is characterized using Fresnel contrast then, unlike in off-axis holography, the groove will not contribute to the contrast, which is only sensitive to high spatial frequency variations in potential. Below a thickness of  $2t_0$  the measured value of  $\Delta V$  will thus be zero (the layer is invisible as no high spatial frequency variations in potential are present). At higher thicknesses,

$$\Delta V = \left(\frac{t - 2t_0}{t}\right)(V_1 - V_2),\quad (4)$$

which again tends towards  $(V_1 - V_2)$  for  $t \gg 2t_0$ . A particularly important parameter is now the product  $(\Delta V \times t)$ ; *whatever* the shape or depth of the groove, a plot of  $(\Delta V \times t)$  against  $t$  has a slope of exactly the desired parameter  $(V_1 - V_2)$  for all specimen thicknesses greater than  $2t_0$ . The intercept of this graph with the  $t = 0$  axis can also provide useful information about the depth and/or the inner potential of the material in the groove (Fig. 8). A similar analysis can be applied to a tilted (or wavy) layer, which can be distinguished from a groove by the fact that  $d$  as well as  $\Delta V$  varies with specimen thickness.  $\Delta V$  now decreases from  $(V_1 - V_2)$  to zero with increasing specimen thickness, while a plot of  $d$  against  $t$  has a slope of  $\sin(\alpha)$  and extrapolates to the origin from large specimen thicknesses (Fig. 8). The parameter  $(\Delta V \times d)$  is always equal to  $w(V_1 - V_2)$ , and  $w$  can be estimated if data from specimen thicknesses below  $w/\sin(\alpha)$  are available.

Figs. 9 and 10 show experimental Fresnel contrast data obtained as a function of specimen thickness using the fitting algorithm illustrated in Fig. 3.

The data in Fig. 9 are taken from the work of Woonbumroong and Boothroyd [39], who measured potential profiles at undoped and 0.8 at% Ho-doped grain boundaries in  $\text{BaTiO}_3$  (shown using open and filled circles, respectively).  $\Delta V$  varies with specimen thickness for both samples and one explanation for this variation is the presence of a surface groove or a tilted layer. (An alternative explanation is the presence of space charge – see below.) For the undoped sample, the measured layer width  $d$  varies linearly with specimen thickness along a line that extrapolates to meet the origin, suggesting that this layer is tilted and that the data points are obtained from a thickness greater than  $w/\sin(\alpha)$ . The slope of the graph would correspond to an effective interface tilt of  $2.2^\circ$ , and the fact that  $(\Delta V \times t)$  and  $(\Delta V \times d)$  are both flat reinforces this interpretation (see Fig. 8). In contrast, for the doped sample the measured width  $d$  is constant with thickness, which is consistent with the presence of a surface groove. The slope of  $(\Delta V \times t)$  is zero, suggesting that the material at the position of the layer has the same mean inner potential as the matrix and that all of the contrast arises from the groove. Fig. 10 shows results plotted as a function of specimen thickness for the three data sets obtained from the  $\text{Fe}_4/\text{Cu}_{13}$  sample described in Fig. 4. Although these data points are noisy because the specimen thickness could not be measured accurately (it would be difficult to assign error bars to the data points), in this case the graphs provide no evidence for the presence of a surface groove, are indicative of waviness corresponding to a small effective tilt of less than  $1^\circ$  and are consistent with the schematic graphs for a tilted layer shown in Fig. 8.

#### 4.2. Space charge

A potential profile may also be affected by the presence of space charge layers at internal interfaces, which are sheets of “bound” charged impurities or defects surrounded by broader distributions of oppositely charge free carriers (Fig. 11a) in a material that remains electrically neutral overall. Such layers can form in materials that include electronic ceramics [40] and epitaxially grown delta-doped semiconductors [41,42]. They provide an

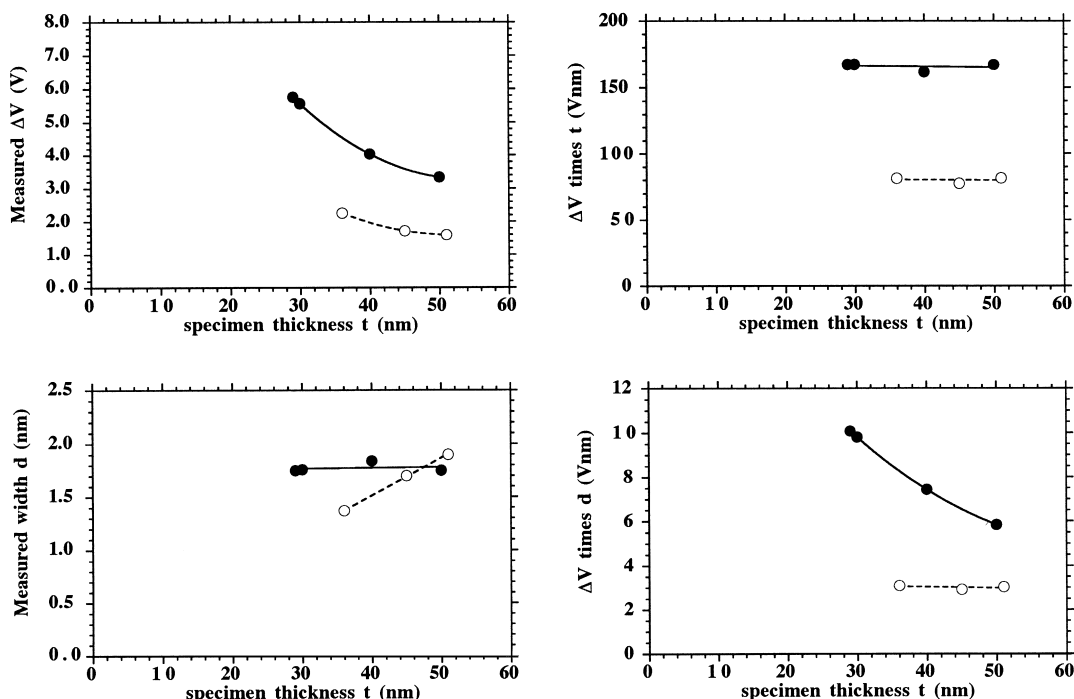


Fig. 9. Experimental Fresnel contrast measurements (using fitting algorithm) of depths and widths of potential wells as function of specimen thickness from undoped and 0.8 at% Ho-doped grain boundaries in  $\text{BaTiO}_3$ , shown using open and filled circles, respectively.

additional contribution to the potential and offer the exciting possibility of quantifying free carrier charge distributions if all other contributions to the potential are negligible or well characterized. Figs. 11b and c show individual and total charge density distributions at a hypothetical space charge layer modeled as a sum of one positive and one negative charge density distribution. The bound and free charge distributions have full-widths at half-maximum of 0.5 and 3.0 nm, respectively, and total charge densities (were each in a single sheet) of  $10^{18} \text{ m}^{-2}$ . The solid and dotted lines correspond to charge distributions that have Gaussian and exponential forms, respectively. (An exponential distribution is predicted using ionic space charge theory, whereas a Gaussian distribution is more representative of a diffusion profile or a ground-state free-carrier wavefunction.) The corresponding electric field and electrostatic potential are shown in Figs. 11d and e for a medium with a dielectric constant  $\epsilon_r$  of 10. The space charge contribution to

the potential is large enough to be detectable and is larger for the exponential than for the Gaussian charge density distributions as a result of the longer tail of the exponential function [43].

Fresnel contrast data from 0, 0.05 and 0.5 wt% Nb-doped  $24^\circ$  [001] tilt boundaries in  $\text{SrTiO}_3$  bicrystals are shown in Fig. 12. Ravikumar et al. [44] reported that the potential profiles at such boundaries can be dominated by contributions from space charge. Two members of a Fresnel defocus series from the 0.5 wt% Nb sample are shown in Figs. 12a and b, and regions from entire defocus series for all three samples are shown in Figs. 12c, d and e for measured sample thicknesses of 42, 37 and 32 nm, respectively. The corresponding line profiles and best-fitting simulations are shown in Figs. 12f–h. The fits were obtained using the algorithm described in Fig. 3, with the fitted potentials at each iteration created from two exponentially decaying charge distributions as would be expected from ionic space charge theory. The real and imaginary



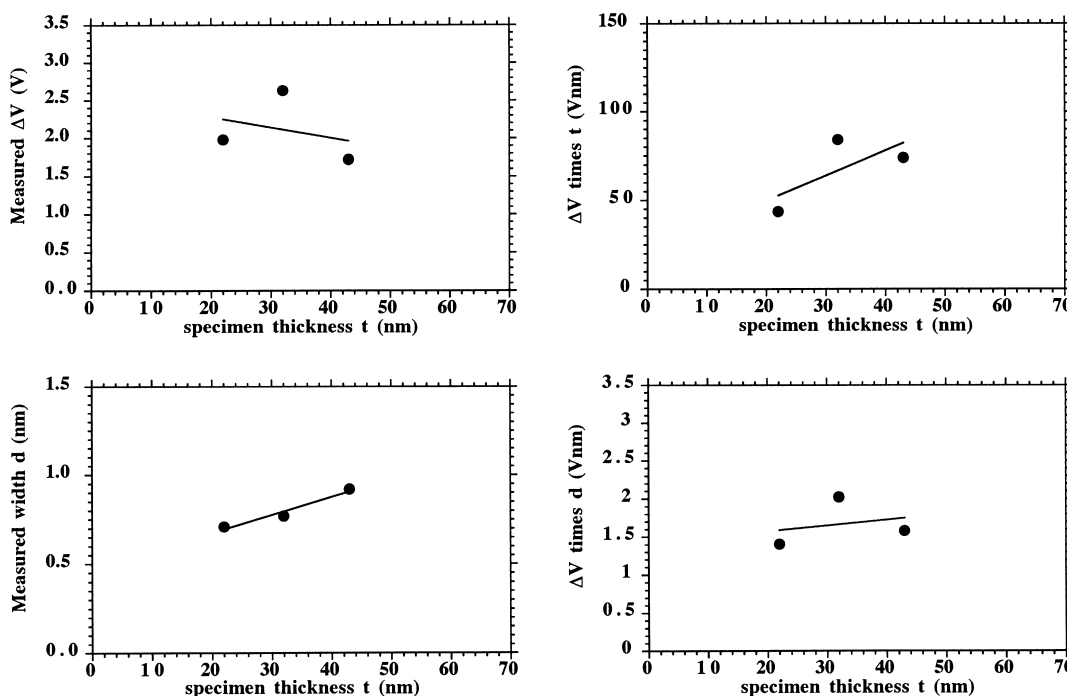


Fig. 10. Experimental Fresnel contrast measurements (using fitting algorithm) of depths and widths of potential wells as function of specimen thickness from  $\text{Fe}_4/\text{Cu}_{13}$  multilayer sample described in Fig. 4.

parts of the fitted potential profiles are shown in Figs. 12i and j, respectively. In order of increasing dopant concentration, the real parts of the potential have depths of 0.34, 1.49 and 0.96 V, and widths of 3.37, 2.02 and 1.35 nm, respectively. The undoped sample exhibits no absorption contrast, whereas the two doped samples show increased scattering to high angles at the position of the layer. A detailed analysis of the possible contributions to the potential [45] shows that the measured profiles cannot be explained on the basis of ionic space charge theory alone and are instead likely to be dominated by changes in scattering factor and density, with a small amount of Nb segregation in the doped samples required to account for the absorptive potentials. This conclusion is in conflict with the work of Ravikumar et al. [44], who interpreted their electron holography results from Mn-doped boundaries in polycrystalline  $\text{SrTiO}_3$  directly in terms of space charge contributions to the potential. However, neither study involved the analysis of data obtained from several specimen thicknesses.

#### 4.3. Fringing fields

Charge redistribution at the surface of a TEM foil is rarely considered. Here, a preliminary discussion of the effect of a free surface on the Fresnel contrast at a space charge layer is presented. Fig. 13a shows the potential profile that would conventionally be included in a simulation of the exponential space charge layer described in Fig. 11, in this case for a sample with a thickness of 50 nm. However, if the charge distribution in Fig. 11b is embedded in a dielectric slab then the potential in Fig. 11e no longer satisfies the boundary conditions to Maxwell's equations at the two specimen surfaces. For a parallel-sided slab, classical image charge theory can be used to calculate the effect of polarization of the specimen surfaces on the potential both inside and outside the material. [46]. The results of such a calculation are shown in Fig. 13b, c and d for the exponential space charge distribution described in Fig. 11, for materials with dielectric constants  $\epsilon_r$  of 1, 10 and 100, respectively.

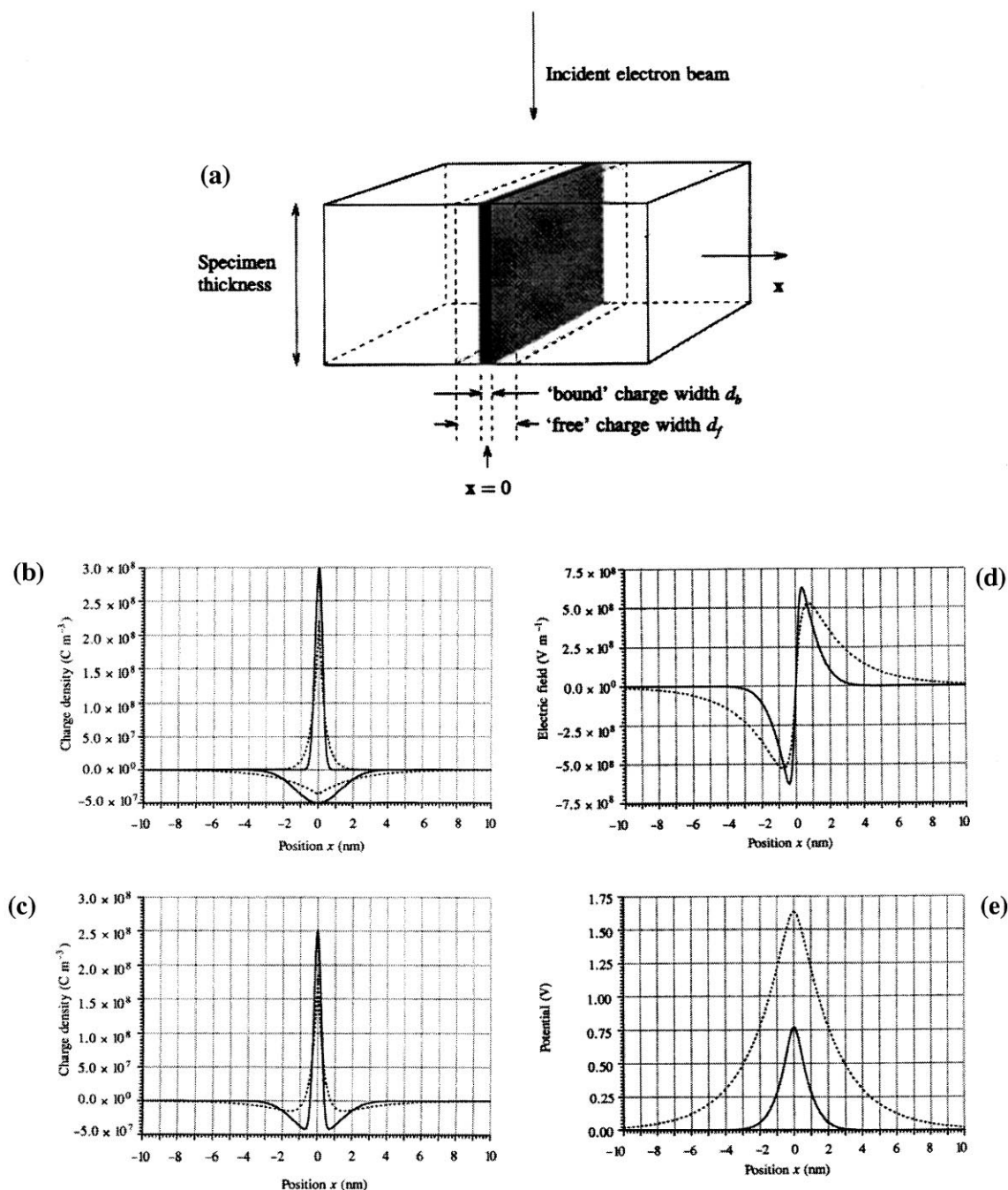


Fig. 11. (a) Schematic diagram showing geometry of cross-sectional TEM sample containing space charge layer; Examples of (b) individual and (c) total charge distributions at space charge layer. 'Bound' and 'free' charge distributions have full-widths at half-maximum of 0.5 and 3.0 nm, respectively. Gaussian and exponential charge distributions are shown using solid and broken line, respectively; (d) electric field and (e) electrostatic potential for charge distributions in c for isotropic material with dielectric constant of 10.

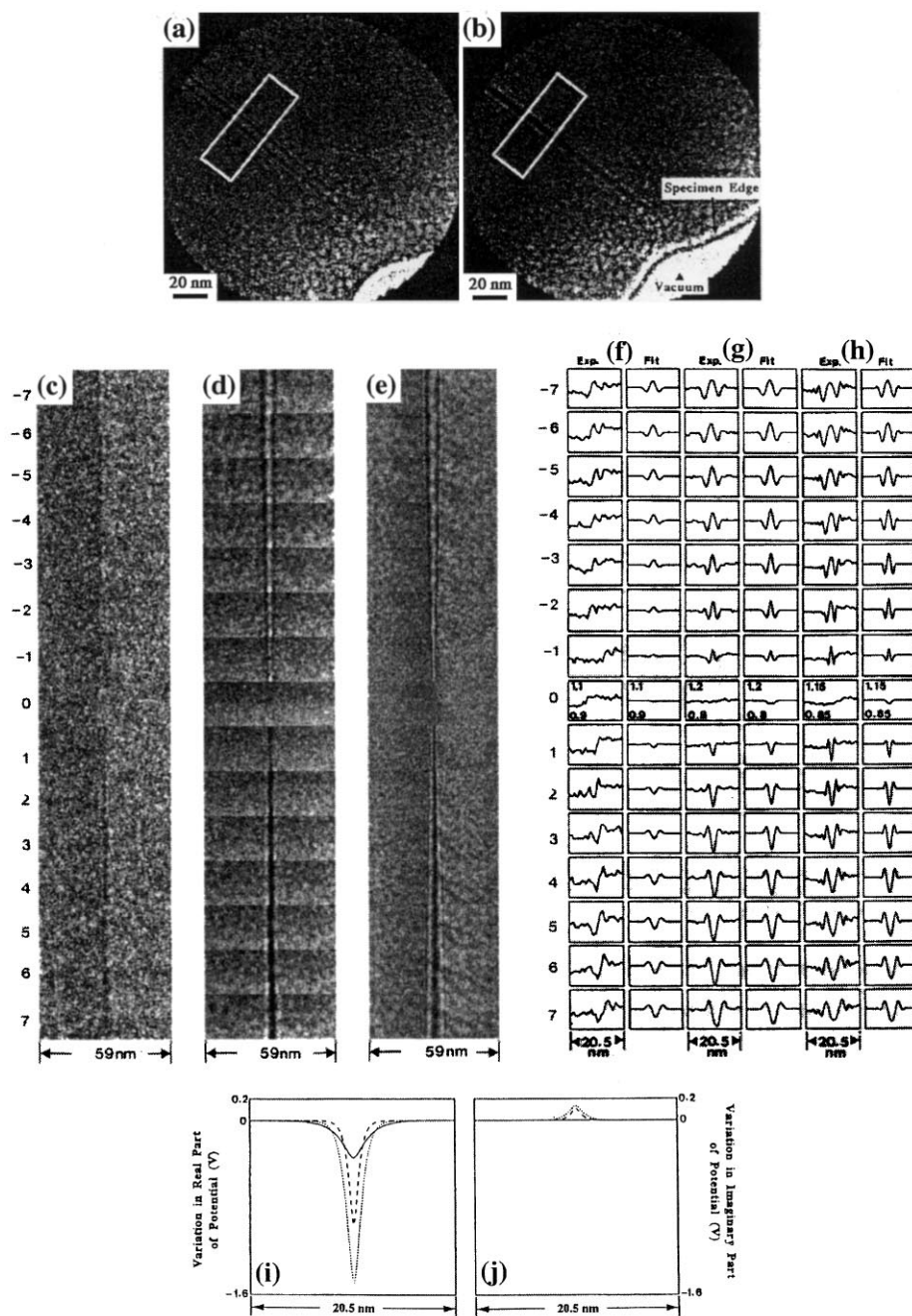


Fig. 12. Fresnel contrast images of  $24^\circ$   $[0\ 0\ 1]$  tilt bicrystal boundary in 0.5wt% Nb-doped  $\text{SrTiO}_3$ , for defocus values of (a) 5660 nm underfocus and (b) 5660 nm overfocus. Intensity in boxed regions was extracted for analysis; Montages showing regions chosen for analysis as function of defocus for (c) undoped, (d) 0.05 wt% Nb-doped and (e) 0.5 wt% Nb-doped samples for measured sample thicknesses of 42, 37 and 32 nm, respectively; (f)–(h) one-dimensional projected Fresnel fringe profiles corresponding to montages shown in c–e, together with best-fitting profiles; Best-fitting potential profiles across boundaries in three specimens examined. Solid, dotted and dashed lines correspond to samples with increasing dopant concentrations. Variation in real and imaginary part of potential are shown in (i) and (j), respectively.

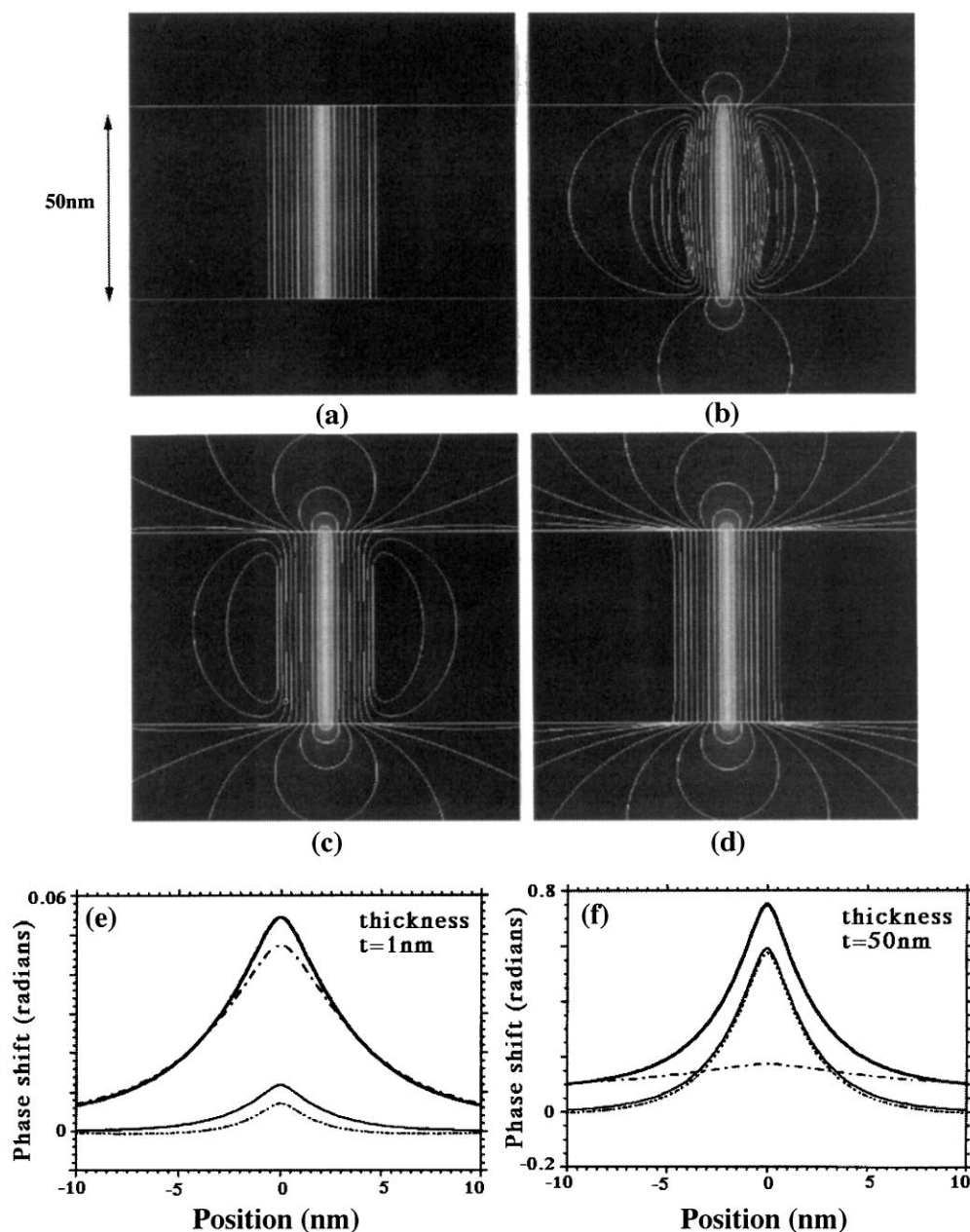


Fig. 13. Electrostatic potentials calculated for exponential space charge distributions shown in Fig. 11b, embedded in dielectric slab of thickness 50 nm. (a) Potential neglecting fringing fields; (b), (c) and (d) show results of image charge calculations for dielectric slabs in which  $\epsilon_r$  is 1, 10 and 100, respectively. Horizontal lines show positions of specimen surfaces. Equipotential contours are spaced geometrically. (see Ref. [45]); (e) and (f) Phase shift experienced by electron on passing through samples in which  $\epsilon_r$  is 10 for thicknesses of 1 and 50 nm, respectively. Image charge calculation of total phase shift and contributions to it from inside and outside sample are shown as thick solid, dotted and dot-dashed lines, respectively. Calculation in absence of fringing fields is shown as thin solid line; (g) simulated through-focal series of images for dielectric slabs of thickness 1 and 50 nm and for dielectric constants shown, using multislice calculation for 200 keV,  $C_s = 2.8$  mm and 0.5 mrad beam convergence. Solid and dotted lines correspond to simulations that neglect and include fringing fields, respectively.

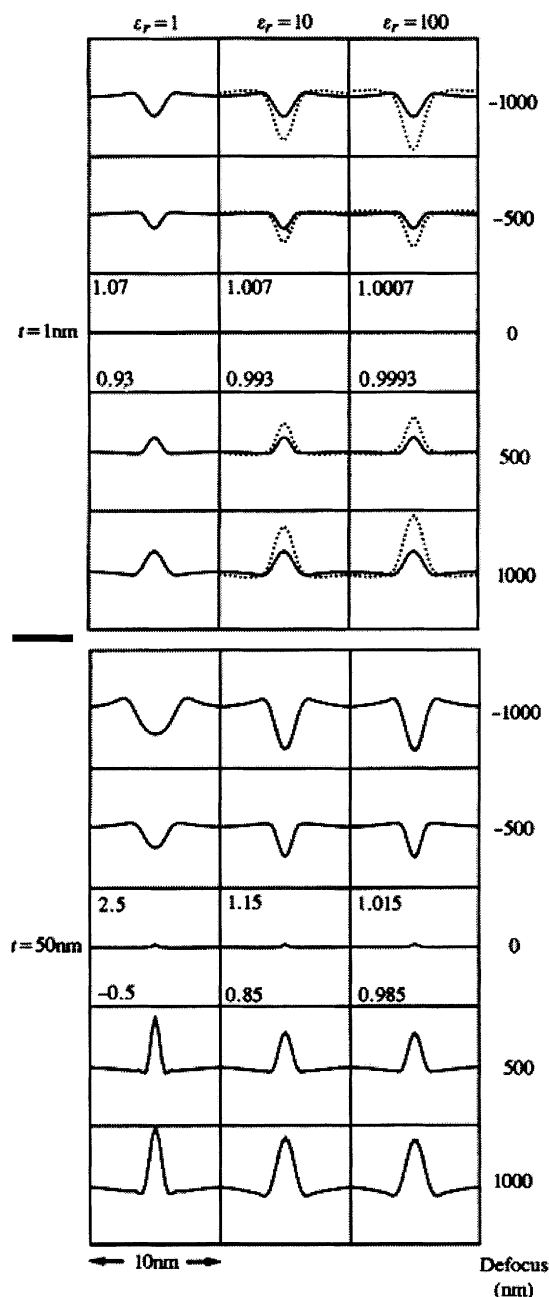


Fig. 13 (continued)

A fringing (or leakage) field is now evident outside the sample. An increase in  $\epsilon_r$  increases the strength of the fringing field. The corresponding effect on the phase shift experienced by a high-energy electron as

it passes through the sample is shown in Figs. 13e and f for a dielectric constant of 10 and for sample thicknesses of 1 and 50 nm, respectively. (The artificially small thickness of 1 nm is included for illustrative purposes only). The total phase shift and the contributions to it from inside and outside the sample are shown as thick solid, dotted and dot-dashed lines, respectively, whereas the calculation in the absence of fringing fields is shown as a thin solid line. For the thinner sample, the phase shift is now dominated by the contribution from outside the foil, while for the thicker sample the external field adds a slowly varying background to the phase shift. The corresponding effect on a Fresnel defocus series is shown for materials with  $\epsilon_r$  of 1, 10 and 100 in Fig. 13g. The effect of the fringing field is only significant at low specimen thicknesses and would cause the width of the potential to be overestimated from its true value. However, it is more important for off-axis holography, which would measure the slowly-varying additional contributions to the phase shift seen in Figs. 13e and f. The effect of the fringing field should be even larger for a sample that contains a p-n junction as a result of the greater width of the depletion region [47].

In practice, the effect of the fringing field may be weaker than suggested by Fig. 13 both because of surface contamination and because surface depletion layers [48] have been neglected. However, the above discussion also suggests the intriguing possibility that, in certain circumstances, similar surface effects on the phase shift may be associated with contributions to the potential from variations in scattering factor.

## 5. Discussion and conclusions

It has been the aim of this paper to describe several recent developments in the application of Fresnel contrast analysis to the characterization of interfaces in the TEM; the most significant of these are the application of automated fitting algorithms and energy-filtered imaging to the determination of best-fitting potential profiles from experimental defocus series. The effects of surface grooves and fringing fields on measured potential profiles have

also been discussed. Possible avenues of future research can be divided broadly into the development of more advanced algorithms for recovering potential profiles, the further understanding of both high- and low-resolution contrast [49,50], and applications to new materials problems. Improved algorithms may involve fitting a larger number of parameters and the use of atomistic multislice calculations. However, it is also essential to understand how to model both absorption [51] and the effect of scattering from amorphous surface layers on the contrast. It may then be possible to compare absolute image intensities (as opposed to image contrast) with simulations. A rigorous treatment of the resolution of a potential profile recovered from a low-resolution focal series of images is also required, as is a better understanding of the relationship between a compositional profile, a potential profile measured in the TEM and a potential profile experienced by a conduction electron [52]. In this context, the relationship between a TEM-measured potential and core-level shifts across interfaces measured using electron energy loss spectroscopy is of great interest. As an alternative to the minimization algorithm described here, many approaches that are currently applied to the analysis of HREM image series would be much more straightforward to apply to the one-dimensional contrast in a low-resolution defocus series obtained from an interface. A similar fitting algorithm could also be applied to the analysis of the Fresnel contrast formed at magnetic domain walls [53,54].

## Acknowledgements

Experimental data were obtained in the Department of Materials Science at the University of Cambridge, primarily under the guidance of the late W.M. Stobbs. This paper is based in part on the work of C.B. Boothroyd, P.D. Brown, C.A. Davis, F. Kara, K.M. Knowles, C.P. Liu, S.J. Lloyd, Z. Mao, D. Özkaya, F.M. Ross, W.O. Saxton, W.C. Shih and A. Woonbumroong. A. Howie, M.R. McCartney, D.D. Perovic, J.C.H. Spence and J.M. Zuo are also thanked for discussions.

## Appendix A

The sequence of input commands and output to the screen for the Semper fitting algorithm used to obtain a best-fitting potential profile to experimental Fresnel contrast profiles:

## References

- [1] F.M. Ross, W.M. Stobbs, *Philos. Mag. A* 63 (1991) 1, 37.
- [2] T. Matsumoto, T. Tanji, A. Tonomura, in: A. Tonomura, L.F. Allard, G. Pozzi, D.C. Joy, Y.A. Ono (Eds.), *Electron Holography*, Elsevier, Amsterdam, 1995.
- [3] J.M. Cowley, *Ultramicroscopy* 41 (1995) 335.
- [4] D.J. Smith, W.J. de Ruijter, M. Gajdardziska-Josifovska, M.R. McCartney, J.K. Weiss, in: A. Tonomura, L.F. Allard, G. Pozzi, D.C. Joy, Y.A. Ono (Eds.), *Electron Holography*, Elsevier, Amsterdam, 1995.
- [5] J.K. Weiss, W.J. de Ruijter, M. Gajdardziska-Josifovska, M.R. McCartney, D.J. Smith, *Ultramicroscopy* 50 (1993) 301.
- [6] W.O. Saxton, T.J. Pitt, M. Horner, *Ultramicroscopy* 4 (1979) 343.
- [7] L.A. Bursill, J.C. Barry, P.R.W. Hudson, *Philos. Mag. A* 37 (1978) 789.
- [8] M. Rühle, S.L. Sass, *Philos. Mag. A* 49 (1984) 759.
- [9] J.N. Ness, W.M. Stobbs, T.F. Page, *Philos. Mag. A* 54 (1986) 679.
- [10] C.S. Baxter, W.M. Stobbs, *Ultramicroscopy* 16 (1986) 213.
- [11] C.B. Boothroyd, A.P. Crawley, W.M. Stobbs, *Philos. Mag. A* 54 (1986) 663.
- [12] W.C. Shih, W.M. Stobbs, *Ultramicroscopy* 32 (1990) 219.
- [13] F.M. Ross, W.M. Stobbs, *Ultramicroscopy* 36 (1991) 331.
- [14] F. Kara, R.E. Dunin-Borkowski, C.B. Boothroyd, W.M. Stobbs, J.A. Little, *Ultramicroscopy* 66 (1996) 59.
- [15] P.A. Doyle, P.S. Turner, *Acta Crystallogr. A* 24 (1968) 390.
- [16] D. Rez, P. Rez, I.P. Grant, *Acta Crystallogr. A* 50 (1994) 481.
- [17] D. Özkaya, W.M. Stobbs, *Inst. Phys. Conf. Ser.* 119 (1991) 217.
- [18] J.M. Cowley, *Acta Crystallogr. A* 44 (1988) 847.
- [19] W.M. Stobbs, W.O. Saxton, *J. Microsc.* 151 (1988) 171.
- [20] M.J. Hytch, M.G. Walls, E. Chassaing, J.P. Chevalier, *Inst. Phys. Conf. Ser.* 153 (1997) 653.
- [21] G.L. Waytena, J. Hren, P. Rez, *J. Appl. Phys.* 73 (1993) 1750.
- [22] C.A. Davis, S.R.P. Silva, R.E. Dunin-Borkowski, G.A.J. Amaratunga, K.M. Knowles, W.M. Stobbs, *Phys. Rev. Lett.* 75 (1995) 4258.
- [23] M. O'Keefe, J.C.H. Spence, *Acta Crystallogr. A* 50 (1994) 33.
- [24] J.C.H. Spence, J.M. Zuo, in: *Electron Microdiffraction*, Plenum, New York, 1992, p. 106.
- [25] W.H. Press, B.P. Flannery, S.A. Teukolsky, W.T. Vetterling, *Numerical Recipes*, Cambridge University Press, Cambridge, UK, 1989.

Frft.spl  
-----

Assumes that the experimental Fresnel fringe profiles are all centred within each picture already & are of an interlayer or a multilayer & not a step or anything more complicated.

Variables that can be set:

\$\$d = \text{diffuseness (default 6)}

\$\$p = \text{magnitude of potential to start from (default 1)}

dpi = flag for displaying output continuously (default 0)

Obtain parameters from an existing variables picture (y/n) ? n  
Number of new variables picture to write to [890]:

First experimental Fresnel fringe profile [11]:  
Sampling density of experimental images in nm/pixel [0.0625]:  
Size of region to compare with simulations [128]:  
Defocus of first picture in nm (underfocus negative) [-1600]:  
Last experimental Fresnel fringe profile [26]:  
Its defocus in nm [1400]:

Assigning memory disk...

Creating a 2D picture containing the experimental profiles...

Outer limits for starting guesses for each parameter:

Lower limit for boundary width in nm [0.5]:

Upper limit for boundary width in nm [1]:

Do we have a well (y) or a barrier (n) ? y

Include absorption in fit (y/n) ? y

Include it as a parameter to try to fit (y/n) ? y

Lower limit (fraction of real potential) [0.06]:

Upper limit [0.12]:

Use a multidimensional simplex minimisation algorithm (y) or vary each parameter in turn in a loop (n) ? y

Total width of simulated profiles in nm [16]:

Corresponding number of pixels (must be a power of 2) [256]:

Specimen thickness in nm [30]:

Slice thickness for multislice calculation in nm [0.2]:

Microscope voltage in kV [200]:

Cs in nm [2]:

Objective aperture radius in mrad [4.18]:

Experimental beam convergence semi-angle in mrad [0.25]:

Focal spread in nm [15]:

Output 17 pictures starting at [100]:

Attempt to fit beam convergence (y/n) ? y

Range on each side of 0.25mrads to consider initially [0.03]:

Attempt to fit starting defocus value (y/n) ? y

Use a cusped exponential space charge potential (y/n) ? n

Itn num	Potential (V)	Fwhm (nm)	Absorption (fraction)	Diffuseness (rms in FT)	Swi (mr)	Goodness of fit
0	-1.1	1.0596	0.06	6	0.22	0.0607237
1	-4.70435	1.0596	0.06	6	0.22	0.00532357
2	-5.01798	1.25371	0.1	5.4	0.11	0.00297037
100	-5.70733	1.12723	0.0844824	5.67318	0.168957	8.94074e-5
200	-5.67485	1.11305	0.0944914	5.75709	0.189265	1.81153e-5
300	-5.6973	1.1118	0.0948455	5.76464	0.193745	1.71286e-5
400	-5.67092	1.10285	0.0998019	5.81947	0.202764	3.80619e-6
505	-5.64365	1.10478	0.0999905	5.80754	0.199339	2.59807e-6

Best-fitting parameters for a convergence of 0.199 mrads are:

Width 1.10nm

Magnitude -5.64V

Diffuseness = convolution of FT by a Gaussian of rad 5.81 pixels

Absorption as a fraction of real part of potential = 0.100.

Starting defocus value = -1499.8nm.

Best-fitting complex potential stored in picture 116.

- [26] J.M. Cowley, *Diffraction Physics*, Elsevier, Amsterdam, 1995.
- [27] P. Nallet, E. Chassaing, M.G. Walls, M.J. Hytch, *J. Appl. Phys.* 79 (1996) 1.
- [28] A.J. den Dekker, A. van den Bos, *J. Opt. Soc. Am. A* 14 (1997) 547.
- [29] S.H. Stobbs, K. Sato, W.M. Stobbs, *Ultramicroscopy* 58 (1995) 275.
- [30] S.J. Lloyd, R.E. Dunin-Borkowski, *Phys. Rev. B* 59 (1999) 2352.
- [31] S.J. Lloyd, *J. Magn. Magn. Mater.* 199 (1999) 671.
- [32] R.F. Egerton, *Electron Energy-Loss Spectroscopy in the Electron Microscope*, Plenum, New York, 1996.
- [33] C.P. Liu, R.E. Dunin-Borkowski, C.B. Boothroyd, P.D. Brown, C.J. Humphreys, *Microsc. Microanal.* 3 (1997) 352.
- [34] Y. Zhu, J. Taftø, L.H. Lewis, D.O. Welch, *Philos. Mag. Lett.* 71 (1995) 297.
- [35] C.P. Liu, R.E. Dunin-Borkowski, W.M. Stobbs, in: *Proceedings of the 11th EUREM*, Dublin, Ireland, *Electron Microscopy 1996*, Vol. 2, Brussels, 1998, pp. 565–566.
- [36] D.R. Rasmussen, C.B. Carter, *Ultramicroscopy* 32 (1990) 337.
- [37] D.B. Williams, C.B. Carter, *Transmission Electron Microscopy*, Plenum, New York, 1996.
- [38] T. Walther, C.B. Boothroyd, C.J. Humphreys, *Inst. Phys Conf Ser.* 146 (1995) 11.
- [39] A. Woonbumroong, C.B. Boothroyd, in: *Proceedings of ICEM 14*, Cancun, Mexico, *Electron Microscopy 1998*, Institute of Physics Publishing, London, UK, 1998, p. 663.
- [40] W. Heywang, *J. Am. Ceram. Soc.* 47 (1964) 484.
- [41] E.F. Schubert, *Delta-doping of Semiconductors*, Cambridge University Press, Cambridge, 1996.
- [42] R.E. Dunin-Borkowski, W.M. Stobbs, in: D.E. Luzzi, T.F. Heinz, M. Iwaki, D.C. Jacobson (Eds.), *Beam–Solid Interactions for Materials Synthesis* Mater. Res. Soc. Proceedings, Vol. 354, Pittsburgh, PA, 1994, pp. 437–442.
- [43] R.E. Dunin-Borkowski, W.O. Saxton, W.M. Stobbs, *Acta Crystallogr. A* 52 (1996) 705.
- [44] V. Ravikumar, R.P. Rodrigues, V.P. Dravid, *J. Am. Ceram. Soc.* 80 (1997) 1131.
- [45] Z. Mao, R.E. Dunin-Borkowski, C.B. Boothroyd, K.M. Knowles, *J. Am. Ceram. Soc.* 81 (1998) 2917.
- [46] R.E. Dunin-Borkowski, W.O. Saxton, *Acta Crystallogr. A* 53 (1997) 242.
- [47] R.E. Dunin-Borkowski, W.O. Saxton, in: D.J. Smith, R.J. Hamers (Eds.), *Atomic Resolution Microscopy of Surfaces and Interfaces*, Mater. Res. Soc. Proceedings, Vol. 466, Pittsburgh, PA, 1996, pp. 73–78.
- [48] D.D. Perovic, M.R. Castell, A. Howie, C. Lavoie, T. Tiedje, J.S.W. Cole, *Ultramicroscopy* 58 (1995) 104.
- [49] C.B. Boothroyd, *J. Microsc.* 190 (1998) 99.
- [50] M.J. Hytch, W.M. Stobbs, *Ultramicroscopy* 53 (1994) 191.
- [51] R.E. Dunin-Borkowski, R.E. Schaublin, T. Walther, C.B. Boothroyd, A.R. Preston, W.M. Stobbs, *Inst. Phys. Conf. Ser.* 147 (1995) 179.
- [52] D.K. Saldin, J.C.H. Spence, *Ultramicroscopy* 55 (1994) 397.
- [53] H. Gong, J.N. Chapman, *J. Magn. Magn. Mat.* 67 (1987) 4.
- [54] S.J. Lloyd, C.B. Boothroyd, P.A. Midgley, *Inst. Phys. Conf. Ser.* 161 (1999) 275.